skb.se

SKB P-23-03

ISSN 1651-4416

ID 2001536

March 2023

POSKBAR-Bentonite Erosion Project

Optimization and validation of a model for quantifying bentonite buffer mass losses due to expansion, erosion, and sedimentation

Arnau Pont

Amphos 21 Consulting S.L.

This report concerns a study which was conducted for Svensk Kärnbränslehantering AB (SKB). The conclusions and viewpoints presented in the report are those of the author. SKB may draw modified conclusions, based on additional literature sources and/or expert opinions.

Data in SKB's database can be changed for different reasons. Minor changes in SKB's database will not necessarily result in a revised report. Data revisions may also be presented as supplements, available at www.skb.se.

This report is published on www.skb.se

Summary

In this work, the general principles and guidelines presented in Pont et al. (2020) and Pont and Idiart (2022) regarding the numerical modelling of bentonite expansion and erosion are further developed. The series of improvements proposed as an extension of the model developed by Neretnieks et al. (2009), Liu et al. (2009) and Moreno et al. (2010) accounting for wall friction and sedimentation have been implemented in COMSOL Multiphysics and tested with relevant experimental data.

In the present work, the model has been further optimized with the prescription of wall friction as a boundary force on a moving bentonite-water interface, which has yielded a significant improvement of the computational performance, a proper prediction of the expansion distance of a wide range of small-scale tests, and a relevant protective effect against erosion. The outcomes in terms of extruded and eroded mass have shown that the correlation between shear stress and sodium concentration at the rim, which has not been yet properly quantified, is of crucial importance for properly describing cases with fracture flow.

Also, a preliminary sedimentation model based on the Brinkmann equations for cases with sloping fractures has been implemented with promising results. The definition of a proper correlation between particle aggregate size and fracture aperture has turned to be the most relevant aspect to be considered in the prediction of the long-term erosion rate in non-horizontal fractures.

Once tested, the model has been upscaled to realistic repository conditions of the KBS-3 concept bentonite buffer intersected by a single horizontal fracture. Again, several flow and fracture configurations have been simulated to provide a preliminary assessment of the long-term buffer integrity and a regression equation for the erosion rate in terms of fracture aperture and flow velocity when glacial groundwater intrudes the bentonite buffer. In this sense, a quadratic dependence with the former and linear with the latter has been found, which differs from the existing models which did not take wall friction into account.

Table of Contents

1 Introduction

In recent years, the mechanisms of bentonite erosion have been intensively investigated to better understand their potential impact on the long-term integrity of the compacted bentonite buffer in the KBS-3 concept over the long term. As part of the EU integrated project BELBaR (Bentonite Erosion: effects on the long-term performance of the engineered Barrier and Radionuclide transport, between 2012 and 2016), several experiments and modelling approaches were conducted and developed. As a result, the erosion models previously used by SKB and Posiva in the initial long-term safety assessments for the final repositories for spent nuclear fuel were further developed and updated. The refined model can be transformed into a relatively simple expression that can be used for quantitative assessments (Neretnieks et al. 2017). However, there are still large uncertainties regarding some of the expansion (or extrusion) and erosion mechanisms, such as gravity, chemical erosion, and friction. These mechanisms still must be properly integrated into a conceptual and computational model.

In this line, the POSKBAR project aimed at quantifying the eroded mass loss of bentonite from the buffer triggered by low salinity groundwater below the Critical Coagulation Concentration (CCC) by two means: experimentally with simplified laboratory tests (Schatz et al. 2013, Schatz and Akhanoba 2017, Appendix B), and numerically with a computational model that overcomes the limitations of the existing approaches. Regarding the latter, Pont et al. (2020) and Pont and Idiart (2022) presented several possible solutions to some of the aforementioned uncertainties in a previous stage of this work, extending the bentonite expansion and erosion model developed by Neretnieks and co-workers (Neretnieks et al. 2009, Liu et al. 2009, Moreno et al. 2010). The main contribution was the inclusion of a wall friction term in the smectite transport equation accounting for the shear resistance exerted by detached flocs at the bentonite-water interface.

In the present work, the model has been further optimized with the prescription of the wall friction term as a boundary force on a moving bentonite-water interface, as well as a preliminary sedimentation model for sloping fractures. The first feature has been implemented with a domain decomposition accounting for two subdomains separated by the rim (Fig. 1-1), which allows segregating the expanding gel from the non-cohesive sol that forms due to the interaction with low salinity groundwater. On one hand, the wall friction divergence term, which corresponds to the formation of shear resistant flocs at the rim, is only applied to the interior domain outside the pellet/buffer. In this way, the term can be precisely decomposed into the proper flux against diffusive expansion at the rim and a bulk term enforcing mass conservation. An on the other, the flow erosion problem (Stokes equations) can be limited to the outer domain and to a Newtonian fluid, thus drastically decreasing the computational cost. The only drawback is the tracking of the rim and having to deal with a moving mesh. All details in this regard are presented in Section 3.

This new version of the model has been thoroughly tested in the present report (Section 4). For this purpose, nine small-scale tests from different laboratories have been simulated (Schatz et al. 2013, Schatz and Akhanoba 2017 and unpublished tests from CIEMAT). They cover a wide parametrization in terms of bentonite type, initial dry density, flowrate, fracture slope and aperture (see Section 2). As it will be shown in Section 4, the wall friction term yields a significant protection against erosion, as it reduces the amount of material being transferred from the expanding disc to the fracture. Although it cannot explicitly describe the aggregation of flocs observed in 0.1 mm fractures leading to the formation of a secondary gel, it might properly describe the blockage at the rim once the bentonite disc stops expanding. In this sense, three tests with this fracture aperture have also been simulated with the model in order to obtain a preliminary assessment of the erosion pattern in such cases.

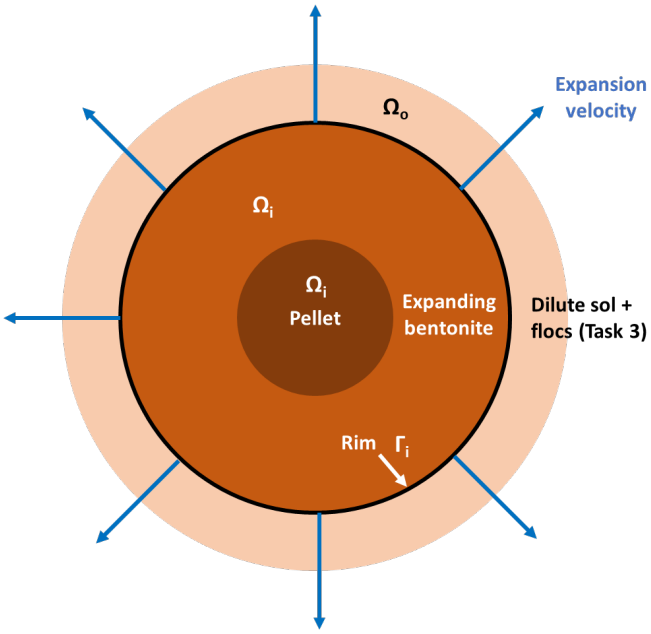

Figure 1-1. *Schematic representation of the domain decomposition and the moving rim.*

In Section 5 the model is applied to the Performance Assessment of the bentonite buffer in the KBS-3 repository under the effect of a single intersecting horizontal fracture with flowing glacial meltwater. The final goal consists in providing a best estimate of the buffer degradation process in critical scenarios involving water salinity below CCC and low calcium sorption. As observed in small-scale tests, these chemical conditions can lead to significant clay mass losses, but the upscaling to repository dimensions assuming normalized erosion rates per unit surface of buffer-fracture interface is not straightforward. Chemical erosion of the buffer is, together with unbounded expansion, one of the major concerns in the long-term safety assessment of a KBS-3 repository. It refers to the decomposition of smectite into colloids due to the presence of groundwater with ionic strength below CCC, and the subsequent material loss because of flow drag or gravity. In this sense, SKB (2004) proposed a mass balance approach for estimating the buffer erosion rate assuming an equivalent flow rate (Q_{eq}) and the dilution of calcite, leading to values ranging from 0.0032 to 0.4 kg·yr^{-1} (3000 to 375,000 years up to loss of integrity damage) depending on the initial calcite concentration. On the other hand, Liu and Neretnieks (2006) revised the previous model assuming real flow rates and replacing calcite by gypsum (0.7 wt.%), which is considered the real driver of calcium concentration in the buffer. In this case, buffer performance was expected to deteriorate beyond 11,000 years (Arthur 2011). However, the SR-Can Safety Assessment (SKB 2006) considered only pure-Na montmorillonite, which is also the focus of the present work. Three different hydrogeological models were considered – continuous porous medium (CPM), fully correlated discrete fracture network (DFN) and semi-correlated DFN, being the latter the worst case with 35% of the deposition holes affected by erosion after 25,000 years (Arthur 2011).

Nowadays, these results are considered rather conservative. In recent years, significant efforts have been devoted to the development of small-scale laboratory tests. A significant resistance to bentonite expansion and erosion was observed in these tests when reproducing the conditions that can lead to an unstable gel. The presence of wall friction and fracture partial clogging due to the formation of secondary gel from flocs formed by the reassembly of detached colloids (Neretnieks and Moreno 2018) requires an extension of the best-estimate numerical models. At the same time, the erosion rate predicted by the coupled model in Neretnieks et al. (2009) was exceeded in one or two orders of magnitude by the upscaling to repository conditions performed with laboratory tests by Smith et al. (2017), who estimated that erosion rates of 1 kg·yr^{-1} may be reached in 4% of the supercontainer sections in the KBS-3H repository concept in Olkiluoto after 1000 years of glacial conditions, although several uncertainties still needed to be addressed.

The present work aims at running a set of relevant parametrizations in terms of salinity, flow velocity and fracture aperture on a realistic buffer geometry crossed by a single horizontal fracture (Section 5). After obtaining all long-term erosion rates (Section 5.1), a multivariable non-linear regression has been performed in Section 5.2. Finally, in Section 6 the main conclusions are listed together with the limitations

of the model and the next steps to be taken for an accurate estimation of the long-term erosion rate in both horizontal and sloping fractures.

For the sake of clarity, a definition of the most relevant concepts related to bentonite-water mixtures is provided next (Neretnieks et al. 2009):

Sheet*:* The smallest building of clay, typically a very thin irregular coin-like sheet, sometimes called lamella, platelet, or flake.

Gel: A dispersion in which the particles cannot move independently of each other. Two main reasons for this are common. Particles are held together by attractive forces. This is the case when they have coagulated in ionic strengths above the critical coagulation concentration. This is called *cohesive* gel. A *repulsive* or *expansive* gel (sometimes referred to as expanding paste in the text) expands until it fills up all the volume available if there are no body forces e.g., gravity that hinders this.

Sol: A dispersion in which the particles are so far apart that they can move independently. In a *stable* sol the repulsive forces are so strong that should particles come near each other by diffusion or due to effects of gravity, they do not combine to form a new particle.

Critical Coagulation Concentration (CCC): Lowest concentration of a certain solute in water (in this case sodium) needed to form a gel.

Chemical erosion: Detachment of smectite particles due to lack of cohesive forces when the ionic strength of water decreases below CCC

Flocculation: Aggregation of detached particles into a segregated gel at the rim (interface between expanded bentonite and water). It might be transported away by seeping water or form a protective layer against further expansion and erosion (secondary gel).

2 Methodology

The description of bentonite expansion and erosion consists of a coupled multiphysics system, characterized by three governing equations: sodium cation transport, smectite expansion, and flow dynamics. All of them are solved in the computational platform COMSOL Multiphysics version 5.6 (COMSOL 2020) based on the finite element method and a staggered coupling scheme, which solves the three equations sequentially up to convergence in the above-mentioned order.

The validation process has consisted in the simulation of 9 small-scale tests from two different laboratories reported by Schatz et al. (2013) and Schatz and Akhanoba (2017), which were already simulated with a previous version of the model (Pont and Idiart 2022), and several new, still unpublished, tests by CIEMAT (Table 2-1). The list accounts for a thorough parametrization of the bentonite buffer-fracture interaction expected in a deep geological nuclear waste repository. Note that the narrowest fracture aperture available, 0.1 mm, has been left out of the scope of the validation. Instead, three cases with this fracture aperture, which has shown in several experiments a different erosion pattern due to partial or complete fracture clogging by secondary gel formation, have been simulated for a preliminary evaluation of the protective effect of the wall friction term presented in Section 3.2 (Table 2-2), as well as the impact of the floc diameter correlation proposed in Section 3.4 on the amount of sedimented mass.

Table 2-1. List of simulated tests for model validation with its main characteristics.

Case	Ref.	Bentonite type	Dry density [kg/m^3]	[Na^+] [mM]	Water inlet velocity [m/s]	Fracture aperture [mm]	Fracture slope (º)	Duration [h]
1	Benero, 23	Nanocor	1700	1	0	0.45	0	720
2	Benero, 24	Nanocor	1700	1	0	0.36	0	720
3	Benero, 28A	Nanocor	1400	1	$5.41\cdot10^{-7}$	0.36	0	1440
4	Benero, 28B	Nanocor	1400	1	$4.08\cdot10^{-7}$	0.45	0	1440
5	Schatz et al. (2013), 3	MX-80	1591	0.03	2.84	1	0	456
6	Schatz et al. (2013), 5	MX-80	1591	0.03	0.38	1	0	672
7	Benero, 15	Nanocor	1400	1	0	0.45	90	720
8	Benero, 16	Nanocor	1400	1	0	0.36	90	720
9	Schatz and Akhanoba (2017), 2	MX-80	1600	0.685	$6.00\cdot10^{-6}$	1	45	720

Table 2-2. List of simulated tests with 0.1 mm fracture aperture with its main characteristics.

Case	Ref.	Bentonite type	Dry density [kg/m^3]	[Na^+] [mM]	Water inlet velocity [m/s]	Fracture aperture [mm]	Fracture slope (º)	Duration [h]
1	Benero, 22	Nanocor	1700	1	0	0.1	0	720
2	Benero, 27	Nanocor	1400	1	$1.50\cdot10^{-6}$	0.1	0	1440
3	DilBi, 5	MX-80	1100	1	$5.59\cdot10^{-5}$	0.1	90	1512

The methodology for the derivation of an expression for the long-term erosion rate in a KBS-3 buffer intersected by a single horizontal fracture in terms of flow velocity, fracture aperture and sodium concentration in water (Section 5) has consisted in the simulation of all possible parametrizations given three relevant values for each variable (27 cases):

Fracture aperture: $\delta_1 = 0.2$ mm, $\delta_2 = 0.4$ mm, $\delta_3 = 1$ mm
Flow velocity: $v_1 = 10^{-7}$ m·s^{-1}, $v_2 = 5 \cdot 10^{-7}$ m·s^{-1}, $v_3 = 3 \cdot 10^{-6}$ m·s^{-1}
Sodium concentration: $c_1 = 1$ mM, $c_2 = 2$ mM, $c_3 = 8$ mM

A fixed value for the initial bentonite dry density of 1600 kg·m^{-3} has been assumed in all cases, as well as homogeneous isotropic smectite diffusion in the buffer.

3 Numerical model

3.1 Model geometry

3.1.1 Small scale tests

The experimental setups developed by CIEMAT, Schatz et al. (2013), Schatz and Akhanoba (2017) and the DilBi test series (Appendix B) are shown schematically in Figure 3-1. In all cases, the assembly includes a planar fracture between two plates, which contains a hole for a pellet of compacted bentonite. The only differences between the different setups are the dimensions of the different components, which are summarized in Table 3-1. A three-dimensional representation of the experiments is considered, though assuming two symmetry planes (Section 3.5). Solving the equations in the initial bentonite domain allows a precise calculation of the swelling pressure in the fracture, which might decrease in small-scale tests due to the small size of the sample.

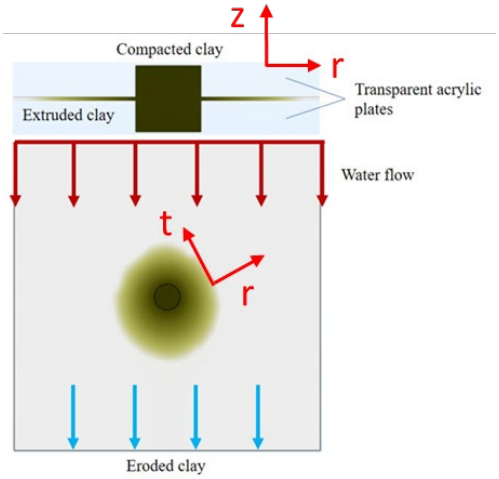

Figure 3-1. *Schematic conceptual model with a planar fracture cutting through a cylindrical bentonite pellet (Neretnieks et al. 2017) showing the radial (r), tangential (t) and vertical (z) directions of the 3D domain.*

Table 3-1. Main features of the different setups corresponding to the small-scale bentonite erosion simulation cases in Section 4.

Tests (reference)	Fracture size [cm]	Pellet shape	Pellet height [cm]	Pellet outer diameter [cm]	Pellet inner diameter [cm]	Initial dry density [kg·m^{-3}]
CIEMAT (unpublised)	17 x 17	cylinder	1	1.9	-	1400
Schatz et al. (2013)	24 x 24	cylinder	2	2	-	1591
Schatz and Akhanoba (2017)	24 x 24	cylinder	2	2	-	1591
Appendix B	17 x 17	Hollow cylinder	1.5	2	0.9	1100

3.2 Repository conditions

For the long-term buffer integrity evaluation analysed in Section 5, a geometrical setup composed by the reference 3D geometry of the installed KBS-3 buffer (SKB 2011) together with a single horizontal fracture 5.5 m x 8 m (Sena et al. 2010) with three different fracture apertures of 1 and 0.4 and 0.2 mm (Fig. 3-2).

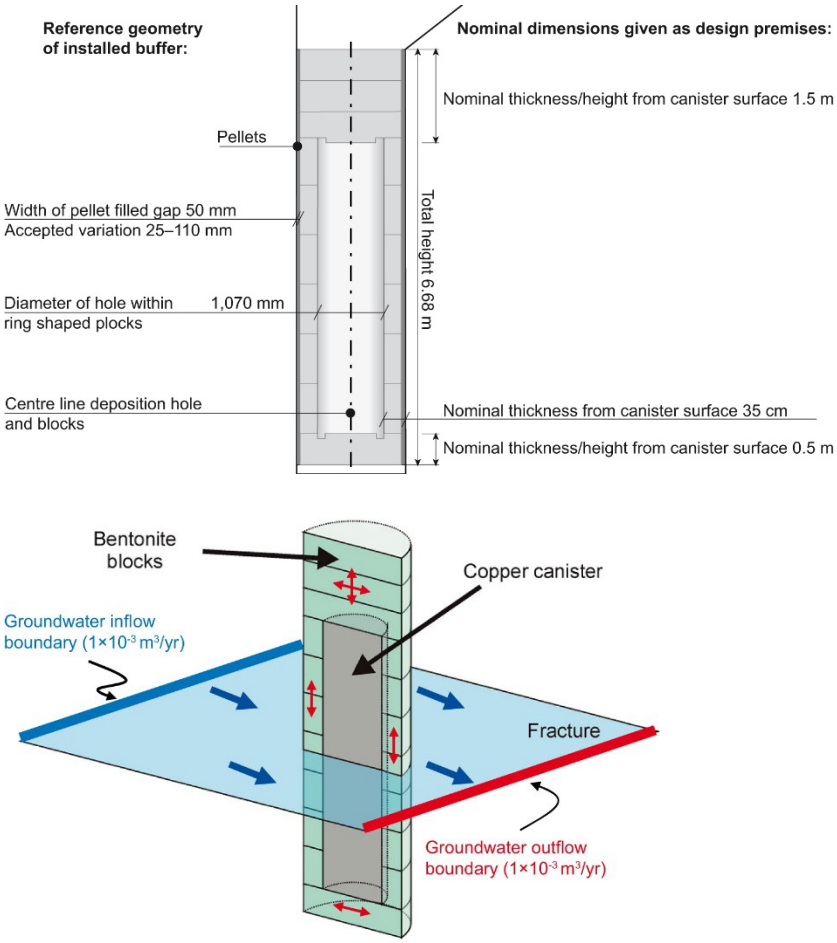

Figure 3-2. *Dimensions of the buffer in the KBS-3 repository (SKB 2011) and schematic representation of a horizontal fracture crossing the bentonite buffer (Sena et al. 2010).*

3.3 Wall friction

The modelling of a resistance against extrusion due to the accumulation of segregated gel at the rim can also be understood as a force applied on a moving boundary. As shown in Pont and Idiart (2022), the added conservative convective term in the model developed by Neretnieks and co-workers (Neretnieks et al. 2009, Liu et al. 2009, Moreno et al. 2010) is only relevant at the vicinity of the rim, although it is applied overall in the fracture as a volume term (equation 3-1). At a conceptual level, this might lead to confusion or even to a misconception of the real force balance taking place at the rim between the expanding gel and the flocculation blocking the fracture.

$$\partial_t \varphi + \vec{u} \cdot \nabla\varphi + \nabla \cdot (\vec{w}\varphi) - \nabla \cdot (D\nabla\varphi) = 0 \qquad \text{Equation 3-1}$$

Since equation 3-1 is to be solved with the finite element method (FEM), its weak form must be derived at the whole domain Ω (equation 3-2), which yields:

$$(\psi, \partial_t \varphi)_\Omega + (\psi, \vec{u} \cdot \nabla\varphi)_\Omega + (\psi, \nabla \cdot (\vec{w}\varphi))_\Omega - (\psi, \nabla \cdot (D\nabla\varphi))_\Omega = 0 \qquad \text{Equation 3-2}$$

If the wall friction and the diffusive terms (third and fourth terms, respectively) are integrated by parts, the natural boundary condition on the domain outer boundaries (Γ) (Neumann fluxes) arise (last term in equation 3-3):

$$(\psi, \partial_t \varphi)_\Omega + (\psi, \vec{u} \cdot \nabla\varphi)_\Omega - (\nabla\psi, \vec{w}\varphi)_\Omega + (\nabla\psi, D\nabla\varphi)_\Omega + (\psi,\ (\vec{w} \cdot \vec{n})\varphi - D\nabla\varphi \cdot \vec{n})_{\Gamma o} = 0$$

Equation 3-3

As the outer boundaries lay in general far away from the expanding disc (Figure 3-1), these fluxes will be negligible, and the last term in equation 3-3 will not be considered. However, this approach leads to an issue that deserve special attention. At a conceptual level, the previous equation applies the wall friction term to the expansive gel, although it is only effective near the rim. One could think about applying this counterforce against expansion as a boundary condition imposed as a diffusive flux on the moving rim as depicted in Fig.1-1, without the necessity of a new term. Nonetheless, this approach would not fulfill mass conservation.

For this purpose, a domain decomposition has been derived. The original domain Ω has been divided into two subdomains separated by the expansion front (rim) referred as Γ (Fig. 1-1). This allows prescribing the wall friction term only in Ω_i outside the pellet so its decomposition with the divergence theorem leads to the precise shear stress on Γ. This blocking effect, together with the motion prescribed to the rim, which will be defined next, will only allow the dilute sol to get into the outer domain Ω_o. Regarding the weak form of the smectite transport problem (equation 3-4), the smectite volumetric fraction is referred by φ, whereas ψ is the corresponding test function, whereas $\vec{u}$ is the flow velocity calculated with the Stokes equation (Section 3.3).

$$(\psi, \partial_t \varphi)_\Omega + (\psi, \vec{u} \cdot \nabla \varphi)_\Omega + (\psi, \nabla \cdot \vec{w}\varphi)_{\Omega i} - (\psi, \nabla \cdot (D \nabla \varphi))_\Omega = 0 \qquad \text{Equation 3-4}$$

The rim moves outwards with a radial velocity defined by the maximum diffusive flux in the expanding inner domain Ω_i, which corresponds to the motion induced by the bentonite swelling pressure (equation 3-5). However, this would lead to unlimited expansion and a wrong location of the shear resistance. Therefore, it is compensated with the shear velocity $\vec{w}$ multiplied by a positioning factor $(\varphi_{\text{rim}}\varphi^{-1})^m$, with parameter $m > 5$ as long as solver convergence is not affected, which will penalize any departure from the prescribed rim concentration φ_{rim}. Apart from a proper placement of the rim, u_{rim} will also be sensitive to flow erosion or sedimentation as they will tend to reduce φ at the rim and therefore u_{rim}.

$$u_{\text{rim}} = \max_{\Omega i}\left(D \nabla \varphi \cdot \vec{n} - \vec{w}\left(\frac{\varphi_{\text{rim}}}{\varphi}\right)^m\right) \qquad \text{Equation 3-5}$$

As a result, the mesh nodes will move at a certain velocity $\vec{v}$ in order to absorb the deformation of the elements caused by u_{rim} (the rim is initially placed 10 mm away from the pellet-water interface). This requires the use of an Arbitrary Lagrangian Eulerian (ALE) frame of reference. Instead of evaluating the equations in a fixed frame, the ALE formulation allows it to have an arbitrary motion, which in the present case is the mesh velocity. After integrating by parts, the diffusive and the shear resistance terms in equation 3-4, one obtains equation 3-6.

$$(\psi, \partial_t \varphi)_\Omega + (\psi, (\vec{u} - \vec{v}) \cdot \nabla \varphi)_\Omega - (\nabla \psi, \vec{w}\varphi)_{\Omega i} + (\nabla \psi, D \nabla \varphi)_\Omega + \left(\psi,\ \varphi(\vec{w} \cdot \vec{n})\right)_\Gamma = 0 \qquad \text{Equation 3-6}$$

The rim velocity (equation 3-5) will make equation 3-6 converge to equation 3-7:

$$(\psi, \partial_t \varphi)_\Omega + (\psi, (\vec{u} - \vec{v}) \cdot \nabla \varphi)_\Omega - (\nabla \psi, \vec{w}\varphi)_{\Omega i} + (\nabla \psi, D \nabla \varphi)_\Omega + \left(\psi,\ \varphi_{\text{rim}}(\vec{w} \cdot \vec{n})\right)_\Gamma = 0 \qquad \text{Equation 3-7}$$

The shear resistance velocity $\vec{w}$ presented by Pont and Idiart (2021) has been restricted to the rim concentration φ_{rim}, which has been set to 0.01 assuming that no yield stress is observed below 3% wt (Neretnieks and Moreno 2018). In other words, it is the lowest smectite volume fracture to yield shear resistance against expansion, and the one which will provide more viscous friction according to the definition of $\vec{w}$ (equation 3-8):

$$|\vec{w}| = \frac{\tau_1\, \delta}{4\eta_{eff}} \xi(r, r_{rim}) \varsigma(r_{rim}) \zeta(\delta) = \frac{k_{HB} |\dot{\gamma}_0|^n\, \delta}{4(\tau_0 |\dot{\gamma}_0|^{-1} + k_{HB} |\dot{\gamma}_0|^{n-1})} \left(\frac{r - r_0}{r_{rim} - r_0}\right)^\beta \left(\frac{r_0}{r_{rim}}\right) \left(\frac{\delta_0}{\delta}\right)^{\frac{1}{n}-1} \qquad \text{Equation 3-8}$$

where τ_0(Pa) is the yield stress τ_1(Pa) is the shear stress after mobilization, δ(m) is the fracture aperture, r(m) is the radius, η_{eff}(Pa·s) is the effective viscosity of the smectite at the rim, $\dot{\gamma}_0$(s^{-1}) is the yield strain

rate and k_{HB} and n are parameters of the Herschel-Bulkley rheological model (Pujala 2014). As conceived by Pont and Idiart (2022), $\vec{w}$ is the virtual average laminar flow velocity between two plates caused by the action of shear stress at the rim. The resulting field defined in the fracture in Ω_i is convoluted by three functions: on one hand ξ restricts $\vec{w}$ near the rim in a sufficiently regular way so it does not compromise continuity in the finite element space. In this sense, β has been preliminarily set to 4. However, this function also determines the thickness of the shear bearing region, which is expected to increase with lower sodium concentration, together with the amount of dilute sol that will diffuse through the rim (chemical erosion). For this reason, β should be expressed in terms of sodium concentration at the rim in a next development stage.

On the other, ς reduces $|\vec{w}|$ proportionally with the expansion distance, since the detached material must fill a longer perimeter, and finally ζ establishes a correlation with the fracture aperture accordingly with the index n of the Herschel-Bulkley rheological model. Taking the widest fracture considered in the calibration ($\delta_0 = 1$ mm) as reference, the relevance of $\vec{w}$ becomes stronger as δ gets smaller. In a linear flow, the exponent would be 1, but in a Herschel-Bulkley the velocity at the centre of a slot shows a slightly different dependence on δ (Neretnieks and Moreno 2018):

$$u_{HB} = \frac{\delta}{\frac{1}{n}+2}\left(\tau_1 \frac{\delta}{K_{HB}}\right)^{\frac{1}{n}} \approx \frac{\delta}{\frac{1}{n}+2}(\dot{\gamma}(\delta^{-1})^n\delta)^{\frac{1}{n}} = \frac{\delta}{\frac{1}{n}+2} f(\delta^{\frac{1}{n}-1}) \qquad \text{Equation 3-9}$$

Equation 3-9 assumes that the strain rate at the centre of the slot is inversely proportional to δ. Bearing in mind that $n = 0.45$ according to Pujala (2014), ζ will be proportional to $\delta^{-1.22}$.
The calibration of the wall friction model in terms of the yields strain rate $\dot{\gamma}_0$ has led to a value of 0.047 s^{-1} for the Nanocor bentonite and 0.055 s^{-1} for the MX-80.

3.4 Flow erosion

With this domain decomposition-based approach, the dilute bentonite sol which is prone to be eroded by a slow fracture flow or by gravity in sloping fractures is only located in the outer domain, for which the solution of the incompressible Stokes equations (equations 3-10 to 3-13) can be restricted to this region. For a bentonite sol below 3% wt., the viscous term is linear (Newtonian fluid), and the relative viscosity follows a cubic correlation (equation 13) in terms of smectite co-volume (sphere in which the smectite coin can rotate freely, Neretnieks et al. 2009) derived by Adachi (1998). According to Moreno et al. (2010), φ_{cov} should be limited to 130% of the coin volume based on the available experimental data (see Appendix A).

$$\rho\partial_t\vec{u} - \nabla\cdot\tau + \nabla p = \vec{0} \qquad \text{Equation 3-10}$$

$$\tau = \eta_w\eta_{rel}\nabla^S\vec{u} \qquad \text{Equation 3-11}$$

$$\rho\nabla\cdot\vec{u} = 0 \qquad \text{Equation 3-12}$$

$$\eta_{rel} = 1 + 1.022\varphi_{cov} + 1.358{\varphi_{cov}}^3 \qquad \text{Equation 3-13}$$

3.5 Sedimentation

The detachment of smectite flocs from the expanded body is a complex phenomenon that cannot be directly described with the previous flow formulation, since the only addition of gravity and buoyancy forces (source term of equation 3-14) would not represent the true motion of detached flocs, which is highly affected by drag force. In this sense, equation 3-15 shows de settling velocity of thin smectite sheets (Neretnieks et al. 2017), derived from the equilibrium with gravity and buoyancy (ρ_w and η_w refer to the density and viscosity of water respectively). However, the translation of this motion into the Stokes equations is not straightforward because they lack a term depending on velocity. For this reason, the Brinkmann equations have been used instead (equation 3-14) with a virtual permeability κ (equation 3-16) derived from the particle velocity described by equation 3-15.

$$\rho\partial_t\vec{u} - \nabla\cdot\tau + \nabla p + \eta_w\eta_{rel}\kappa^{-1}\vec{u} = \vec{g}(\rho - \rho_w) \qquad \text{Equation 3-14}$$

$$u_p = \frac{g(\rho-\rho_w){d_p}^2}{18\eta_w} \qquad \text{Equation 3-15}$$

$$\kappa = \frac{\eta_{rel} {d_p}^2}{18}$$ Equation 3-16

$$d_p = d_{p0} \left(\frac{\delta}{\delta_0}\right)^{\alpha}$$ Equation 3-17

The model still must undergo a calibration process in order to determine d_{p0}, the average particle aggregate diameter for apertures with $\delta \geq \delta_0$ (free sedimentation). A preliminary value of 2.5 μm has been assumed (Al-Risheq et al. 2021). On the other hand, the dependence between particle diameter and fracture aperture still needs to be assessed (equation 3-17) and will be crucial for describing the low erosion rates observed in 0.1 mm fractures, where the motion and the size of smectite flocs is strongly constrained by the walls. This can lead to the formation of a secondary gel which might even clog the fracture. According to Neretnieks et al. (2017), based on experiments, the settling velocity of large coin-like agglomerates with 1% by volume smectite in a vertical slit shows a quadratic dependence respect to the aperture. Since velocity depends on ${d_p}^2$, α will be 1 in all cases. However, as it will be observed in Sections 4 and 5, this correlation still needs to be revised.

3.6 Computational model

The setup shown in Fig. 3-1 has been implemented in the COMSOL Multiphysics (COMSOL 2020) computational platform in a 3D geometry. Taking profit from the planar and vertical symmetries, only a quarter of the original domain has been considered. With that, a more refined radial mesh of 50,000-112,000 linear elements has been generated, depending on the fracture aperture (Fig. 3-3).

As previously stated, a moving mesh algorithm has been solved for minimizing element distortion caused by the motion of the rim (Γ). Foreseeing the expansion beyond the initial position of the rim (1 cm from the pellet), the interior domain has been carefully refined in order to prevent resolution losses due to the expected element size growth. Despite this extra computational cost, the final version of the model drastically outperformed the previous ones. Except the sedimentation cases, which still need to be refined, the simulation of all other tests has taken less than 1 hour

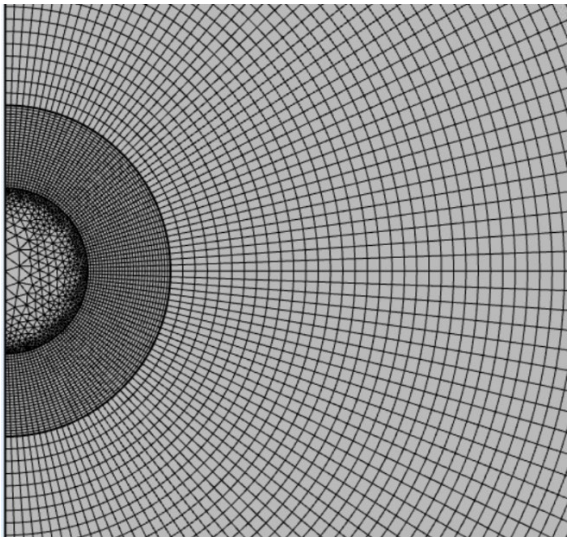

Figure 3-3. *Finite Element mesh in COMSOL. The areas subject to more deformation have been specifically refined.*

Regarding the upscaled model to repository dimensions (Fig. 3-4), the increase in computational cost with respect to the short small-scale tests have limited both mesh refinement and the total simulation time that can be considered. A single simulation up to 100,000 years could be affordable with the last version of the model, but a parametric sweep for a multivariable regression as presented next would be excessively time consuming. From this reason, only 1-10 years from the onset of glacial meltwater arrival have been considered, up to the time needed for expansion and erosion to reach pseudo-steady state conditions.

The most relevant dimensions of the buffer have been obtained from SKB (2011). Like in the models developed for the small-scale tests, only a quarter of the geometry has been considered due to symmetry, and a radial mesh of linear elements with specific refinement of the expanding region and the initial bentonite-water interface has been generated (Fig. 3-4). This has led to a model size ranging from 146,000 to 220,000 elements depending on the fracture aperture.

In the present case, special attention has been paid to the positioning of the rim being the nearest possible to the prescribed rim concentration (0.01 in volume fraction), otherwise significant deviations in the calculation of the long-term erosion rate might occur.

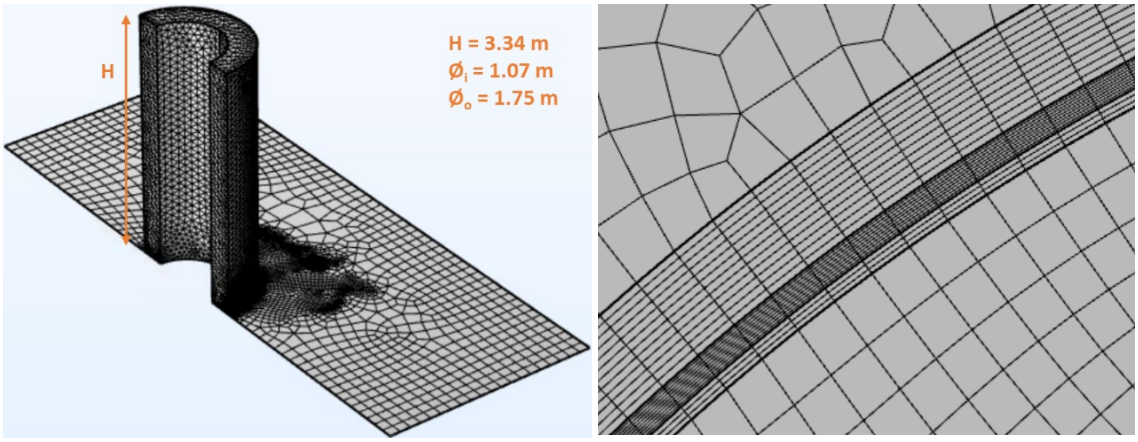

***Figure 3-4**. Computation model after considering vertical and fracture midplane symmetries (left). Mesh refinement at the buffer-fracture interface with special focus on the expanding region (right).*

4 Results. Validation of the model

In this section, the main results of the tests described in Table 2-1 in terms of expansion and mass distribution in the pellet and the fracture, including eroded mass, are presented and compared to experimental measurements. First, a summary is shown in Table 4-1. Cases 1 and 2, which are purely expansive, are properly described by the model, which yields an accurate estimate of both the extruded mass and the final expansion distance. In cases 3 and 4, which are equivalent to the previous ones except for a smaller initial dry density, a slow fracture flow and twice the duration, the model provides a conservative estimation of both expansion and pellet mass reduction. The reason behind this disagreement might be the value of the function β in equation 8 (wall friction term), which should be adapted to a lower sodium concentration at the rim due to advective transport. This would enhance sol diffusion through the rim thus increasing the erosion rate and decreasing the expanded mass as observed in the experimental results. Another possible improvement might consist in adapting the sol viscosity correlation to the Nanocor clay, since this disagreement has not been observed in cases 5 and 6, which correspond to the MX-80 bentonite. In these two cases, the only observed discrepancy between experimental and modelled results is the final expansion distance in case 5, the test with a highest flowrate. This might be related to the onset of shear resistance due to floc formation at the rim. The model considers this force from the very beginning of bentonite expansion, but in reality, this phenomenon is not instantaneous and would allow for a short initial period of free expansion. Since this delay has not been included in the model, the fracture flow manages to immobilize the expanding front at a very early stage. Except for this only case, Fig. 4-1 shows that the model provides an accurate description of expansion in a wide range of scenarios.

Finally, the preliminary sedimentation results, corresponding to case 7 to 9, show a promising performance of the model with both Nanocor and MX-80 clays. Still, the last case, which yields the highest sedimentation rate due to a bigger fracture aperture, confirms that the model presented in Section 3.4 needs further refinement regarding the average smectite sheet diameter.

Table 4-1. Main results in terms of bentonite expansion and final mass balance for the validation cases.

	Ref.	Expansion [cm]		Pellet mass [g]		Fracture mass [g]		Eroded mass [g]	
Case		Exp.	Calc.	Exp.	Calc	Exp.	Calc.	Exp.	Calc.
1	Benero, 24	3.77	3.81	3.22	3.33	1.49	1.49	0	0
2	Benero, 23	3.95	4.02	2.90	2.98	1.89	1.83	0	0
3	Benero, 28A	4.02	5.08	2.85	1.92	0.71	1.93	0.40	0.11
4	Benero, 28B	4.56	4.94	2.81	2.22	0.86	1.66	0.30	0.08
5	Schatz et al. (2013), 3	2.25	1.00	4.61	4.16	0.68	0.29	4.73	5.55
6	Schatz et al. (2013), 5	2.30	2.34	4.90	4.14	0.91	1.40	4.19	3.46
7	Benero, 15	3.65	3.63	2.54	2.49	0.89	1.41	0.099	0.06
8	Benero, 16	3.77	3.42	2.81	2.78	0.87	1.14	0.046	0.04
9	Schatz & Akhanoba (2017), 2	Experim. erosion rate: $2.65 \cdot 10^{-9}$ kg/s				Calculated erosion rate: $1.43 \cdot 10^{-9}$ kg/s			

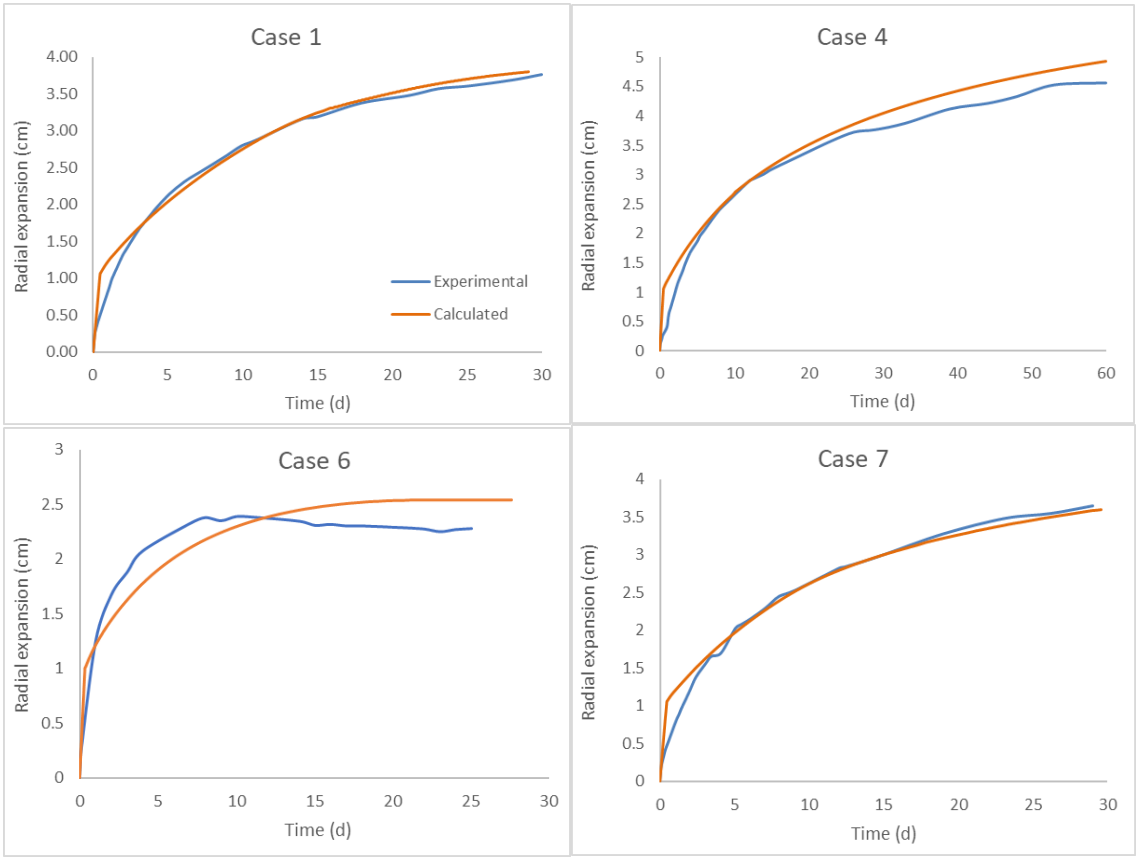

Figure 4-1. *Time evolution of the expansion radius in four of the simulated tests.*

5 Upscaling to repository conditions

5.1 Simulation results

An early analysis of the results showed an unclear correlation between erosion rate and sodium concentration in fracture water (Table 5-1). The main reason behind this unexpected outcome is the rheological model applied to calculation of shear resistance at the rim, since it does not take into account the salinity of water (Pujala 2014, Neretnieks and Moreno 2018). This prevents the diffusion of a higher quantity of dilute sol through the rim when the sodium concentration decreases, which is something that can be clearly observed when the wall friction term is switched off and diffusivity only depends on the attractive and repulsive forces at the nanoscale. A thorough discussion on this topic can be found in Section 3.2, where a possible way to overcome this issue has also been proposed. For this reason, the dependence of the erosion rate on this variable has been initially left out of the calculation process, reducing the regression to fracture aperture and flow velocity (9 cases).

As expected, results in Table 5-1 show a clear dependence of the erosion rate on flow velocity and fracture aperture, which will be quantified in Section 3.2. It can be also observed that in all cases the predicted erosion rate is significantly lower than the values provided by the upscaling of small-scale tests proposed by Smith et al. (2017). If the results were to be projected to 1 million years, only the case with the widest fracture and the highest velocity (20 g/year) would lead to the failure of the buffer. However, the results obtained by Smith et al. (2017) corresponded to non-horizontal fractures, which have not been considered in the present work.

Another important outcome of the study is the prediction of the final bentonite expansion distance. In all cases expansion stops within 1 to 2 cm away from the buffer-fracture interface. Of course, this result might change once the wall friction term is correlated with sodium concentration at the rim.

Table 5-1. Erosion rate after reaching pseudo-steady (g/year).

	δ_1	δ_2			δ_3		
	c_1	c_1	c_2	c_3	c_1	c_2	c_3
v_1	0.01	0.30	0.30	0.34	0.86	--	--
v_2	0.26	0.82	--	--	4.19	--	--
v_3	1.49	3.94	--	--	20	21.3	17.9

5.2 Long-term buffer erosion rate for single horizontal fractures

From the data compiled in Table 5-1, a multivariable non-linear regression using Vlab has been performed. As a result, a quasi-linear correlation between the erosion rate *ER* (g/year) and the fracture flow velocity *v* (m/s) has been found, as well as a quasi-quadratic dependence on the fracture aperture δ (m) (Equation 5-1).

$$ER\ (g/year) = 1.993 \cdot 10^{13} \cdot v^{1.0484} \cdot \delta^{2.0156} \qquad \text{Equation 5-1}$$

This outcome contrasts with the regression performed by Moreno et al. (2010) on its own expansion and erosion model, which found a linear correlation with δ and a dependency on $v^{0.41}$, whereas the analytical expressions derived by Neretnieks et al. (2010) using the *Qeq* concept and Neretnieks et al. (2017) in his two-region model for a single bentonite buffer intersected by a horizontal fracture with water of glacial origin yielded a correlation with $v^{1/2}$ and linearity respect to the fracture aperture, too. In the present model, the linear correlation with velocity might suffer significant changes once the impact of sodium concentration at the rim is included, since the latter variable will not be independent from the former. However, the quadratic correlation with the fracture aperture is clearly given by the effect of the wall friction term. The previous models only rely on the bentonite-water surface area, which grows linearly with δ, but in the present case the contribution of the shear resistance at the rim, which decreases with $\delta^{-1.22}$, must also be considered.

The error minimization criterion is not disclosed by the calculation tool. For this reason, the coefficient determination R^2, which measures the quality of the adjustment by the regression curve, has been calculated obtaining a value of 0.75. However, case (c_1, v_1, δ_3) turns to be a clear outlier in terms of regression error. After removing its contribution to the calculation of R^2, this coefficient increases up to

0.97. For the sake of simplicity, equation 5-1 has been transformed into natural exponents while maximizing the R^2 coefficient (equation 5-2), which has grown up to 0.95 with the full data set and to 0.98 without the outlier case. Moreover, it has been expressed in terms of the buffer diameter (D_b) so the expression can also be applied to small-scale tests. The 3D plots of equations 5-1 and 5-2 and the corresponding 2D projections are shown in Figures 5-1 and 5-2 respectively.

$ER\ (g/year) = 8.0 \cdot 10^{12} \cdot v \cdot \delta^2 = 4.57 \cdot 10^{12} \cdot D_b \cdot v \cdot \delta^2$ Equation 5-2

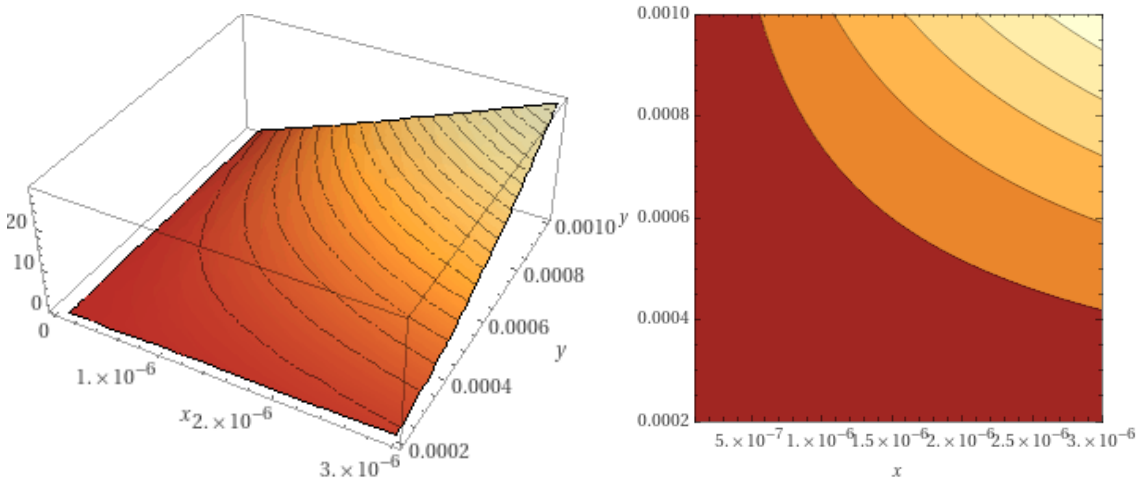

***Figure 5-1**. 3D plot of equation 1 with isolines (left) and 2D projection (right) with x = v and y = δ.*

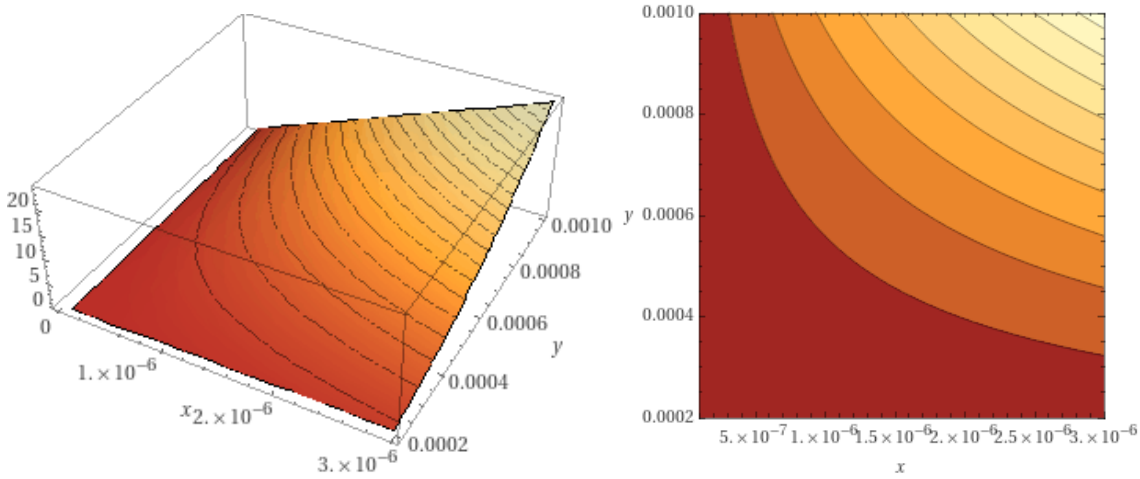

***Figure 5-2**. 3D plot of equation 2 with isolines (left) and 2D projection (right) with x = v and y = δ.*

Finally, a verification case with an alternative parametrization (δ = 0.6 mm and $v = 10^{-6}$ m/s) has been calculated in order to evaluate the accuracy of the regression by equation 5-2. An erosion rate of 2.65 g/year has been obtained, in front of the 2.88 g/year provided by equation 5-2.

6 Conclusions and future work

The new version of the model prescribes shear resistance of segregated gel as a boundary force at the rim, which is tracked with a moving finite element mesh with a self-regulating algorithm. In spite of these major conceptual and implementation changes, the limitation of bentonite expansion due to the effect of fracture walls has been properly described for small-scale tests performed with different fracture aperture and slopes, flow regimes, salinities and bentonite dry densities for both sodium bentonites Nanocor and MX-80. Furthermore, the presented implementation has also led to a further reduction of the computational cost, which in turn has allowed a much more straightforward upscaling of the model to repository conditions.

Regarding bentonite erosion due to fracture flow, the model has yielded a proper quantification of the lost mass in two cases with MX-80 bentonite, whereas the erosion of Nanocor clay has been significantly underestimated in the three cases with horizontal fracture. This disagreement should be attributed to two reasons: the wall friction term not being expressed in terms of the sodium concentration at the rim, and the use of the same sol viscosity correlation in the Stokes equations for both clays.

The sedimentation model presented in Section 3.4, although at a preliminary development stage, has yielded promising results. The two cases with vertical fracture and Nanocor clay (0.36 and 0.45 mm) have been properly described by the model except for a slight underestimation of the eroded mass. However, the erosion rate for the MX-80 bentonite in a 1 mm fracture has been significantly underpredicted, from which it can be concluded that the reference particle diameter should be revised.

The preliminary results corresponding to the cases with 0.1 mm fractures have provided relevant insights. On one hand, the correlation between wall friction and fracture aperture considered in all other cases has proved to be unsuitable for 0.1 mm fractures, as it strongly underestimates expansion and erosion. On the other, the sedimentation particle size correlation with fracture aperture used in the validation cases with promising outcomes, has led to the opposite effect in a narrow vertical fracture.

Overall, it can be concluded that the current model can be trustfully applied to any scenario with horizontal fractures (> 0.1 mm) provided the rheological information of the dilute sol is available. Further work is still needed in modelling wall friction and sedimentation in 0.1 mm fractures.

The predicted long-term erosion rate for the KBS-3 buffer concept intersected by a single horizontal fracture has been significantly lower than the upscaling from small-scale tests performed by Smith et al. (2017) in all considered cases. However, the latter focused on sloping fractures, which have not been considered in the present study, where sedimentation is expected to be the main erosion driver. On the other hand, the results have shown an unclear correlation between erosion rate and sodium concentration in the fracture water, which contrasts with the drastic mass loss increase observed experimentally when sodium concentration tends to zero. For this reason, the initial 27-case parametrization based on flow velocity, fracture aperture and sodium concentration has been reduced to the first two variables and 9 cases.

The multivariable non-linear regression performed over all the calculated erosion rates has provided a clear correlation with the considered variables: linear respect to flow velocity and quadratic respect to fracture aperture with a coefficient determination R^2 of 0.95. This result differs from previous models, which had predicted a linear correlation with the fracture aperture and a squared root dependency on the flow velocity. Whereas the correlation with velocity is expected to change once the sodium concentration at the rim is included in the regression, since they are not independent, the quadratic dependence on the fracture aperture can be explained by the effect of the wall friction term.

Based on the presented outcomes, the first next step will consist in expressing the wall friction term presented in Section 3.2 in terms of the sodium concentration at the expanding front. This will allow a more conservative assessment of the most critical cases. The second one will focus on the development of a suitable sedimentation model for sloping fractures. A preliminary version with promising results has already been presented in the present work, but a deeper understanding of the correlation between the average smectite aggregate size and fracture aperture is still needed. Once this model is validated with experimental results from small-scale tests, a new regression expression of the buffer erosion rate for non-horizontal fractures in terms of slope, sodium concentration and fracture aperture will be derived.

References

SKB's (Svensk Kärnbränslehantering AB) publications can be found at www.skb.com/publications.

Adachi Y, Nakaishi K, Tamaki M, 1998. Viscosity of dilute suspension of sodium montmorillonite in an electrostatically stable condition. Journal of Colloid and Interface Science 198, 100–105.

Al-Risheq D I, Nasser M S, Qiblawey H, Hussein I A, Benamor A, 2021. Choline chloride based natural deep eutectic solvent for destabilization and separation of stable colloidal dispersions. Separation and Purification Technology 255, 117737.

Alonso U, Missana T, García Gutiérrez M, Morejón J, Mingarro M, Fernández A, 2019. CIEMAT studies within POSKBAR project. SKB TR-19-08, Svensk Kärnbränslehantering AB.

Arthur R, 2011. Handling of hydrogeochemical relations in erosion and swelling pressure models for the buffer and backfill. Part I: A review of surface-chemical concepts used in models of buffer erosion. STUK-TR 10, Radiation and Nuclear Safety Authority, Finland.

COMSOL, 2020. COMSOL Multiphysics®. Version 5.6. Stockholm: COMSOL AB.

Liu L, Neretnieks I, 2006. Physical and chemical stability of the bentonite buffer. SKB TR-06-103, Svensk Kärnbränslehantering AB.

Liu L, Moreno L, Neretnieks I, 2009. A dynamic force balance model for colloidal expansion and its DLVO-based application. Langmuir 25, 679–687.

Moreno L, Neretnieks I, Liu L, 2010. Modelling of erosion of bentonite gel by gel/sol flow. SKB TR-10-64, Svensk Kärnbränslehantering AB.

Neretnieks I, Liu L, Moreno L, 2009. Mechanisms and models for bentonite erosion. SKB TR-09-35, Svensk Kärnbränslehantering AB.

Neretnieks I, Liu L, Moreno L, 2010. Mass transfer between waste canister and water seeping in rock fractures. Revisiting the Q-equivalent model. SKB TR-10-42, Svensk Kärnbränslehantering AB.

Neretnieks I, Moreno L, 2018. Some mechanisms that influence bentonite erosion in a KBS-3 repository – an exploratory study. SKB TR-18-13, Svensk Kärnbränslehantering AB.

Neretnieks I, Moreno L, Liu L, 2017. Clay erosion – impact of flocculation and gravitation. SKB TR-16-11, Svensk Kärnbränslehantering AB.

Pont A, Coene E, Idiart A, 2020. Bentonite erosion project. Preliminary study for the numerical simulation of bentonite erosion. SKB P-20-16, Svensk Kärnbränslehantering AB.

Pont A, Idiart A, 2022. Numerical Model for the Quantification of Buffer Bentonite Mass Losses due to Expansion, Erosion and Sedimentation Posiva SKB Report 13. Svensk Kärnbränslehantering AB.

Pujala R K, 2014. Dispersion stability, microstructure and phase transition of anisotropic nanodiscs. Cham: Springer International Publishing.

Schatz T, Akhanoba N, 2017. Bentonite Buffer Erosion in Sloped Fracture Environments. Posiva 2016-13, Posiva Oy, Finland.

Schatz T, Kanerva N, Martikainen J, Sane P, Olin M, Seppälä A, Koskinen K, 2013. Buffer Erosion in Dilute Groundwater. Posiva 2012-44, Posiva Oy, Finland.

Sena C, Salas J, Arcos D, 2010. Aspects of geochemical evolution of the SKB near field in the frame of SR-Site. SKB TR-10-59, Svensk Kärnbränslehantering AB.

SKB, 2004. Interim process report for the safety assessment SR-Can. SKB R-04-33. Svensk Kärnbränslehantering AB.

SKB, 2006. Long-term safety for KBS-3 repositories at Forsmark and Laxemar – a first evaluation. Main Report of the SR-Can project. SKB TR-06-09, Svensk Kärnbränslehantering AB.

SKB, 2011. Long-term safety for the final repository for spent nuclear fuel at Forsmark. Main report of the SR-Site project. SKB TR-11-01. Svensk kärnbränslehantering AB.

Smith P, Schatz T, Reijonen H, Hellä P, 2017. Chemical Erosion and Mass Redistribution of Bentonite in a KBS-3H Repository. Posiva 2016-12, Posiva Oy, Finland.

Appendix A

The equations of the KTH model corresponding to the derivation of the smectite diffusion coefficient (Liu et al. 2009), which have been implemented in COMSOL, are presented below:

$$\partial_t \varphi = -\vec{u}\nabla\varphi + \nabla \cdot (D_F \nabla\varphi)$$ Equation A-1

$$D_F = \frac{\chi(1-\varphi)^{1.6}}{f}$$ Equation A-2

$$h = \left(\frac{\varphi_{max}}{\varphi} - 1\right)\delta_p$$ Equation A-3

$$f = \left[6\pi\eta_w r_{eq} + V_p k_0 \tau^2 a_p^2 \eta_w \frac{\varphi}{(1-\varphi)^2}\right]$$ Equation A-4

$$\chi = k_B T + \left(h + \delta_p\right)^2 \left(\frac{\partial F_A}{\partial h} - \frac{\partial F_R}{\partial h}\right)$$ Equation A-5

$$\frac{\partial F_A}{\partial h} = -\frac{A_H S_p}{2\pi}\left[h^{-4} - 2\left(h + \delta_p\right)^{-4} + \left(h + 2\delta_p\right)^{-4}\right]$$ Equation A-6

$$\frac{\partial F_R}{\partial h} = -4\kappa c R T S_p \tanh y^m \left[\cosh y_\infty^m \sinh\left(\frac{y_\infty^m}{2}\right) + \frac{1}{\kappa h}\sinh y_\infty^h + \frac{2}{(\kappa h)^2}\sinh\left(\frac{y_\infty^h}{2}\right)\right]$$ Equation A-7

$$y^m = \operatorname{asinh}\left[2\sinh y_\infty^m + \frac{4}{\kappa h}\sinh\left(\frac{y_\infty^h}{2}\right)\right]$$ Equation A-8

$$y_\infty^m = 4\operatorname{atanh}\left[\tanh\left(\frac{y_\infty^0}{4}\right)\exp\left(-\frac{\kappa h}{2}\right)\right]$$ Equation A-9

$$y_\infty^h = 4\operatorname{atanh}\left[\tanh\left(\frac{y_\infty^0}{4}\right)\exp(-\kappa h)\right]$$ Equation A-10

$$\kappa = \left(\frac{2F^2 c z^2}{\varepsilon_0 \varepsilon_r R T}\right)^{1/2}$$ Equation A-11

$$y_\infty^0 = 2\operatorname{asinh}\left(\frac{s_0}{2}\right)$$ Equation A-12

$$s_0 = \frac{zF\sigma^0}{\varepsilon_0 \varepsilon_r \kappa R T}$$ Equation A-13

The smectite sol viscosity correlation presented by Adachi et al. (1998) has also been implemented:

$$\eta_{rel} = 1 + 1.022\varphi_{cov} + 1.358\varphi_{cov}^3$$ Equation A-14

$$\varphi_{cov} = \frac{2}{3}\frac{\left(D_P + 2m\kappa^{-1}\right)^3}{D_p^2 \delta_p}$$ Equation A-15

Notation	Property	Value and/or unit
k_B	Boltzmann's constant	$1.380 \cdot 10^{-23}$ J/K
r_{eq}	Equivalent radius of non-spherical particles	63.66 nm
F	Faraday's constant	96 485 C/mol
m	Fitting parameter in co-volume fraction	1
R	Gas constant	8.314 J/(K mol)
A_H	Hamaker constant	$2.5 k_B T$
$k_0 \tau^2$	Kozeny's constant	5, 13
φ_{max}	Maximum volume fraction of smectite	1
ε_0	Permittivity of vacuum	$8.854 \cdot 10^{-12}$ F/m
ε_r	Relative permittivity of water	78.54
D_P	Smectite particle diameter	200 nm
δ_p	Smectite particle thickness	1 nm
a_p	Specific surface area per unit volume of particles	$2/\delta_p$ m^2/ m^3
S_p	Surface area of smectite particle	$3.1415 \cdot 10^{-14}$ m^2
σ^0	Surface charge of particles	-0.131 C/m^2
T	Temperature	298.15 K
z	Valence of counterion	1
η_w	Viscosity of water	$1.002 \cdot 10^{-3}$ N s/m^2
φ	Volume fraction of smectite – variable	-
V_p	Volume of the smectite particles	$3.1415 \cdot 10^{-23}$ m^3

Appendix B

Case 3 (Table 2-2) simulate an experimental test performed by A-Insinöörit Civil Oy laboratory in Finland (unpublished work), which has been developed in collaboration with Posiva. This test is briefly presented in this appendix. Case 3 corresponds to Test 5.

Its main objective was to evaluate the performance and robustness of a measurement system for studying clay mineral erosion in artificial factures under flowing synthetic groundwater conditions. Several tests in different setups were performed to reproduce the conditions that might reduce dry density of bentonite.

The test studied here (denoted as Test 5) was conducted with an artificial fracture setup with an annular sample compartment at the centre of the test cell. Thus, swelling in this test is radial. The clay was homoionic Na-montmorillonite with initial nominal dry density of 1100 kg/m^3. The sample was placed in a specimen cylindrical compartment with 20 mm in diameter. The test cell was placed vertically, and the flow of 1 mM NaCl solution was imposed from top to bottom (maintained constant with a peristaltic pump). The solution was prepared using deaerated and deionized water. Some initial air pockets were observed, that subsequently disappeared due to the constant flow of deaerated solution. The solution was shielded from the atmosphere by means of collapsible containers (Hydra-Pak Shape-shiftTM) to avoid lowering of pH from the interaction with atmospheric CO_2. More details about the experiment are included in Table 2-2.

The test ran for a period of 63 days and upon termination two main results were obtained: a limited expansion radius of approximately 8.9 mm, and an early decrease of the erosion rate. This apparently reduced mass loss was tightly related to the partial clogging of the fracture due to the coagulation of smectite flocs in the form of a secondary gel.